ACS APPLIED MATERIALS & INTERFACES

Research Article

www.acsami.org

Individually Stabilized, Superparamagnetic Nanoparticles with Controlled Shell and Size Leading to Exceptional Stealth Properties and High Relaxivities

Andrea Lassenberger,[†] Andrea Scheberl,[†] Andreas Stadlbauer,[‡,§] Alexander Stiglbauer,[‡] Thomas Helbich,[‡] and Erik Reimhult*[,†]

[†]Department of Nanobiotechnology, Institute for Biologically Inspired Materials, University of Natural Resources and Life Sciences, Muthgasse 11, 1190 Vienna, Austria

[‡]Department of Biomedical Imaging and Image-guided Therapy, Division of Molecular and Gender Imaging, Medical University Vienna, Waehringer Guertel 18-20, 1090 Vienna, Austria

[§]Department of Neurosurgery, University of Erlangen-Nürnberg, Schwabachanlage 6, 91054 Erlangen, Germany

Supporting Information

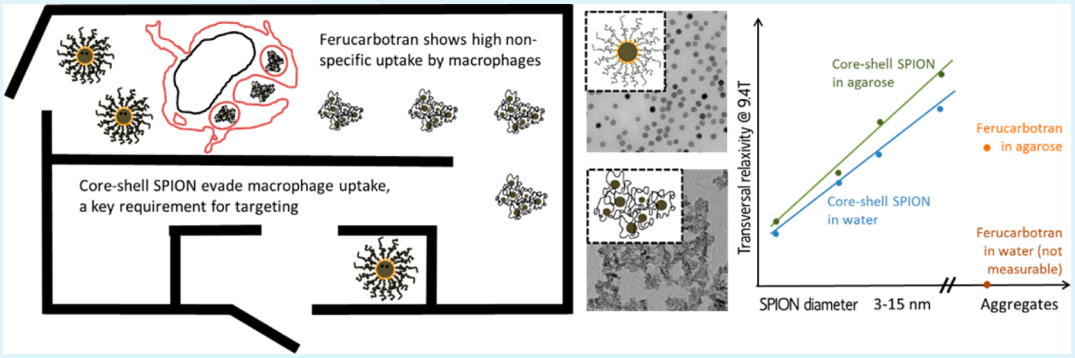

ABSTRACT: Superparamagnetic iron oxide nanoparticles (SPION) have received immense interest for biomedical applications, with the first clinical application as negative contrast agent in magnetic resonance imaging (MRI). However, the first generation MRI contrast agents with dextran-enwrapped, polydisperse iron oxide nanoparticle clusters are limited to imaging of the liver and spleen; this is related to their poor colloidal stability in biological media and inability to evade clearance by the reticuloendothelial system. We investigate the qualitatively different performance of a new generation of individually PEG-grafted core−shell SPION in terms of relaxivity and cell uptake and compare them to benchmark iron oxide contrast agents. These PEG-grafted SPION uniquely enable relaxivity measurements in aqueous suspension without aggregation even at 9.4 T magnetic fields due to their extraordinary colloidal stability. This allows for determination of the size-dependent scaling of relaxivity, which is shown to follow a d^2 dependence for identical core−shell structures. The here introduced core−shell SPION with ∼15 nm core diameter yield a higher R_2 relaxivity than previous clinically used contrast agents as well as previous generations of individually stabilized SPION. The colloidal stability extends to control over evasion of macrophage clearance and stimulated uptake by SPION functionalized with protein ligands, which is a key requirement for targeted MRI.

KEYWORDS: *core−shell, superparamagnetic iron oxide nanoparticles, targeted magnetic resonance imaging, size-dependent relaxivity, macrophage nanoparticle uptake*

1. INTRODUCTION

Superparamagnetic iron oxide nanoparticles (SPION) have emerged as promising T_2 magnetic resonance imaging (MRI) contrast agents (CAs). Some products have been FDA approved, such as carboxydextran-coated Ferucarbotrans and dextran-coated Ferumoxides primarily designed for imaging of the liver.[1] Pure iron oxide nanoparticles stabilized by biodegradable and biocompatible polymers are particularly interesting as contrast agents for medical applications due to their inherent low toxicity[2,3] and relative ease of synthesis.[2,4] However, by 2009, the commercial production of FDA-approved SPION-CAs ceased due to unexpectedly poor performance in clinical trials and severe side effects, such as lumbar and leg pain in 2−10% of patients, which led to very limited use by radiologists.[1,5,6] Ferumoxtran-10 SPION were designed for lymph node imaging[7] but failed in pivotal studies due to lack of statistically relevant benefit for significance and nonspecificity where the application of the CA led to false

Received: October 11, 2016
Accepted: January 10, 2017
Published: January 10, 2017

DOI: 10.1021/acsami.6b12932
ACS Appl. Mater. Interfaces 2017, 9, 3343−3353

positive results and unnecessary surgeries.[8,9] Today, only Ferucarbotran is available in a limited number of countries.[10]

The biodistribution and performance of nanomaterials in vivo depends foremost on their ability to remain undetected by the reticuloendothelial system (RES) that quickly sequesters foreign substances from the body and on their ability to avoid getting filtered out by organs such as the kidney, liver, and spleen. This property of evasion, which is dependent on size and surface properties of nanomaterials, is often referred to as "stealth" and it is required for active targeting to be achieved.[11,12] SPION, such as Ferucarbotrans and Ferumoxides, are characterized by very high macrophage uptake; this limited their use to imaging the liver and spleen, in which they were deposited after being quickly cleared from the blood by the RES.[2,13] The fast clearance ($t_{1/2}$ < 10 min for Ferucarbotran)[5,14] and distribution to the liver was a consequence of limited stealth capability rather than active targeting using biomolecular interactions specific to the target tissue.[15] In contrast to this, nanomaterials for active targeting require (a) low to negligible nonspecific uptake and clearance by the RES, leading to long blood circulation times that allow for effective transport of the nanoparticles to the desired site (e.g., tumor tissue), and (b) the possibility to bind to tissue-specific markers in the human body through specific biomolecular interactions by, e.g., antibodies coupled to the nanoparticles.[16]

The reason for the lacking capability to avoid nonspecific interactions and cell uptake of the first generation Ferucarbotran and Ferumoxide contrast agents can be attributed to the undefined structure of the shell, which consists of physically adsorbed polymers such as carboxydextran,[5] dextran,[17,18] and other carbohydrate derivatives[3] wrapped around polydisperse iron oxide cores. The resulting matrix-like structure has multiple cores distributed in dynamically rearranging polydisperse particle aggregates. The average CA size is, therefore, typically an order of magnitude larger than the nominal SPION core size.[19]

Since then, efforts were made to design a second generation of SPION with polydisperse cores that are individually stabilized by end-grafting a hydrophilic polymer chain via a defined anchor group.[20] This results in a defined core−shell architecture with irreversibly grafted shells of defined thickness; it allows for keeping a small overall CA size, tailoring interactions with biomolecules and cells, and opens the door to further functionalization for specific cell and tissue targeting. These properties are crucial to improve medical applications and can only be achieved if the shell is dense and covalently anchored in contrast to the physisorbed dynamic shells of the first generation CAs.[20] This second generation has not yet made it into clinical testing, but since the colloidal interactions of nanoparticles are strongly determined by nanoparticle size, curvature, and ligand density, we and others[21−24] have tried to further refine this design concept toward truly monodisperse core−shell SPION with controlled and designed shell compositions.[25,26] A third generation CA with monodisperse iron oxide cores and well-defined shells grafted with a nitrodopamine anchor to the SPION surface was, therefore, recently reported by us; these SPION are synthesized by methods that can be scaled up for volume production of SPION-CA designed for specific targeting.[27,28] So far, the size of these superparamagnetic, single-crystalline, PEGylated, core−shell SPION was limited to ∼10 nm in diameter, which, for single core−shell SPION, is likely to lead to lower relaxivities in MRI than for the first generation CA due to the low magnetic moment of nonaggregated SPION in this size range.

In this work, we present the successful synthesis of nitrodopamine (NDA)-anchored poly(ethylene glycol) (PEG)-stabilized[27,29] single-crystalline, and spherical magnetite cores up to 14.4 nm in diameter. We could for the first time investigate the performance of individually stabilized core−shell SPION with a controlled variation of size and controlled colloidal stability as MRI contrast agents, including their ability to evade uptake by phagocytic cells typical for the RES. These SPION are shown to exhibit exceptional ability to suppress nonspecific interactions and cell uptake, negligible toxicity, and very high transversal relaxivities that scale with the SPION core diameter. The highest relaxivities reported to date for individually stabilized core−shell SPION were recorded for the novel 14.4 nm PEGylated SPION, and the SPION were observed without aggregation even in a 9.4 T magnetic field, adding drastically different capabilities compared to the first generation CA.[30]

2. EXPERIMENTAL SECTION

Materials. All Chemicals (see the SI for details) were purchased from Sigma-Aldrich, all solvents from Roth and PEG from JenKem, and used as received without further purification.

Transmission Electron Microscopy (TEM) and Analysis. TEM studies were performed on an FEI Tecnai G2 20 transmission electron microscope operating at 160 kV or 200 kV for high resolution imaging. Samples were prepared by dropping toluene dispersions (as-synthesized SPION) or aqueous dispersions (PEGylated SPION) onto a 300-mesh carbon-coated copper grid and subsequently evaporating the solvent in air. Size distributions were evaluated using the Pebbles[31] software package with a local intensity-model fitting algorithm. For each batch, approximately 900 SPION from both high and low resolution TEM were sampled for size determination by Pebbles.

Thermogravimetric Analysis (TGA) and Differential Scanning Calorimetry (DSC) Measurements. Thermograms were recorded on a Mettler-Toledo TGA/DSC 1 STAR System in the temperature range 25−650 °C with a ramp of 10 K/min in a synthetic air stream of 80 mL/min in order to ensure complete combustion of ligands as NDA was found to polymerize upon pyrolization under N_2. 70 μL aluminum oxide crucibles were filled with 0.5−1.5 mg of sample, and the total organic content (TOC) was evaluated as the mass loss fraction at 500 °C by horizontal setting.

Dynamic Light Scattering (DLS). DLS data were recorded on a Malvern Zetasizer Nano-ZS at 20 °C. Measurement conditions: Material Fe_3O_4, dispersant water (0.89 mPa·s, RI = 1.33), 3 individual measurements with 13 runs at 10 s each. All SPION dispersions were measured at a concentration of 1 mg_{Fe}/mL. Importantly, multiple scattering was not observed at this Fe concentration.

Statistical Analysis. Analysis of variance for the cell uptake experiments was done by 1-way ANOVA for significance levels of p < 0.001, p < 0.01, and p < 0.05. Tukey's method was applied for the comparison of means and Levenes's test was chosen for testing equal variance.

SPION Synthesis. SPION (3−10 nm in diameter) stabilized with oleic acid (OA) were synthesized by thermal decomposition of an iron precursor according to a slightly modified heat-up procedure described by Hyeon et al.;[32] e.g., for 10.6 nm diameter SPION, a mixture of 50 mL of dioctylether (Oct_2O) and 7.04 mL of OA was heated to 100 °C under N_2. Next, 1 mL of iron pentacarbonyl ($Fe(CO)_5$) was injected rapidly and the reaction mixture was heated to 290 °C with a temperature ramp of 3 °C/min. After aging for 1 h, the SPION dispersion was allowed to cool to room temperature and precipitated thrice with ethanol (EtOH) from toluene in order to remove excess OA. The size was controlled by the $Fe(CO)_5$:OA ratio; details can be found in the Supporting Information (Table S1). Four different core

DOI: 10.1021/acsami.6b12932
ACS Appl. Mater. Interfaces 2017, 9, 3343−3353

sizes were selected for the investigation of the MRI signal and two sizes for the cell uptake experiments.

Synthesis of the large 14.4 nm in diameter SPION followed a modified two-step method introduced by Park et al.[33] First, the iron-oleate complex (Fe-oleate complex) was synthesized by mixing 3.6 g of $FeCl_3 \cdot 6H_2O$ and 12.17 g of sodium oleate in 26.7 mL of EtOH, 20 mL of Milli-Q, and 46.6 mL of *n*-hexane. The mixture was refluxed at 70 °C for 4 h and allowed to cool to room temperature. After washing the organic layer thrice with 30 mL of Milli-Q, the solvent was removed and the Fe-oleate complex was obtained as reddish viscous material in 98% yield. In a second step, SPION were synthesized as follows: 6.6 g of Fe-oleate complex was mixed with 0.56 mL of OA and 25 mL of Oct_2O. The mixture was heated to 100 °C under a N_2 atmosphere to remove residual water. After heating to 290 °C with a temperature ramp of 3 °C/min, the mixture was aged for 90 min and cooled to room temperature. SPION size was controlled by the Fe-oleate:OA ratio. The workup was identical as that for smaller SPION.

Synthesis of Nitrocatechol Ligands. 6-Nitrodopamine-hydrogensulfate (NDA-HSO_4) was synthesized according to the literature with slight modifications.[34] NDA-PEG (5 kDa or 10 kDa) was synthesized by (1-cyano-2-ethoxy-2-oxoethylidenaminooxy)-dimethylamino-morpholino-carbenium hexafluorophosphate (COMU)-mediated peptide-coupling reactions[35,36] and confirmed by FT-IR and NMR (see the SI for experimental details).

Ligand Exchange. PEGylated SPION were synthesized and purified as published previously.[27] Typically, 1.2 g of OA capped SPION were mixed with 20 mL of DMF and 0.7 g of nitrodopamine-poly(ethylene glycol) (NDA-PEG(5 kDa) or NDA-PEG(10 kDa)) and sonicated for 26 h at 35 °C. For the biotinylated SPION, a mixture of NDA-PEG(5 kDa) and NDA-PEG(5 kDa)-Biotin was used in the desired amount to reach a calculated number of either 4 or 90 biotin molecules per SPION. Consequently, the SPION were washed thrice with *n*-hexane to extract released OA and the solvent was evaporated. SPION were lyophilized and purified from excess ligands and physisorbed OA by precipitation from EtOH/petrolether 1:1 and magnetic decantation. The procedure was repeated 5 times until the organic content was constant and all excess ligands were removed. The purified PEGylated SPION were lyophilized for long-term storage as a dark-brown powder in 96% yield with respect to the initially applied cores. SPION of all sizes were coated with NDA-PEG(5 kDa); the large 14.4 nm SPION were coated with NDA-PEG(5 kDa) and NDA-PEG(10 kDa).

Nonfunctionalized, only PEGylated SPION are denoted as SPION-PEG(5 kDa) or SPION-PEG(10 kDa); PEGylated + biotinylated SPION are denoted as SPION-NDA-PEG-4B (4 biotin/SPION) or SPION-NDA-PEG-90B (90 biotin/SPION). Hydrophilic core−shell SPION were characterized by IR, TEM, and TGA. SPION stock solutions of 1.0 mg Fe/mL in Milli-Q were prepared and stored at 4 °C. The Fe concentration of the stock solutions was confirmed by a Ferrozine test.[37]

Streptavidin/Avidin Functionalization. To trigger the non-specific uptake by macrophages, biotinylated SPION were decorated with streptavidin or avidin. Briefly, 0.25 equivalents (equiv) of streptavidin or avidin (with respect to the amount of biotin on the SPION) was added to the SPION in Milli-Q water and shaken for 24 h at 4 °C to complete the binding (see the SI for details). All resulting dispersions had an Fe concentration of 1.0 mg/mL. The resulting SPION are denoted as SPION-NDA-PEG-4B-Strept, SPION-NDA-PEG-4B-Avidin, SPION-NDA-PEG-90B-Strept, or SPION-NDA-PEG-90B-Avidin.

Cell Uptake and Lysis. U937 cells were grown in RPMI-1640 medium supplemented with 10% (v/v) heat-inactivated fetal calf serum, 2 mM L-glutamine and 10 mM HEPES buffer, antibiotics, and MEM nonessential amino acids in a humidified 5% CO_2 atmosphere at 37 °C.

For uptake, macrophages U937 were incubated with SPION for 20 h. Six well plates were inoculated with 4×10^6 cells in total 4 mL of medium. Next, 50 μL of the 1 mg Fe/mL SPION stock solutions was added, and the cells were incubated for 20 h. The blind was incubated with 50 μL of Milli-Q water. After uptake, cells were spun down and the pellet was washed twice with PBS in order to remove SPION that had not been taken up by the cells.

For iron quantification, a modified protocol of the Ferrozine test was used.[37] The cell pellets were lysed in 1 mL of 50 mM NaOH for 20 h at RT. After centrifugation and short sonication in order to destroy DNA strands, the supernatant was used for determination of the iron content.

For each type of SPION, at least 3 wells were prepared in parallel and at least 3 independent tests were performed, making a total of minimum 9 data points for each type of SPION.

Iron Quantification/Ferrozine Test. A 200 μL portion of the lysates was mixed with 200 μL of 10 mM HCl and 200 μL of releasing agent (equal volumes of 1.4 M HCl and 4.5% $KMnO_4$ mixed and used immediately) and incubated for 2 h at 60 °C. After cooling down to room temperature, 60 μL of detection reagent (6.5 mM FerroZine and neocuproine in 1 M ascorbic acid + 2.5 M ammoniumacetate) was added and allowed to react for 30 min at RT. As control sample, the SPION dispersion was used. Extinction of the Ferrozine-iron complex was measured at 550 nm, 3 individual measurements for each well. 5−150 μM $FeCl_3$ was used for calibration.

Protein Quantification/Bradford Assay. Protein determination was done using Sigma Bradford assay according to the manufacturer's directions. 20 μL of the lysate was mixed with 500 μL of Bradford reagent and incubated for 15 min at RT. Extinction was measured at 595 nm. 2.5−10 μg of BSA (dissolved in 50 mM NaOH) was used for calibration.

Embedding of Cells and Thin Sectioning for TEM Analysis. Embedding of cells was done in Epon epoxy resin according to a modified protocol of Glauert and Lewis.[38] Briefly, cells after uptake were washed twice in PBS, fixed in fixative containing 2.5% glutardialdehyde, 2.5% paraformaldehyde, 2.5 mM $CaCl_2$, and 1% tannic acid in 0.1 M sodium cacodylate pH 7.4 for 4 h. Fixation was repeated with fixative without tannic acid for 20 h at 4 °C. After washing with sodium cacodylate, followed by distilled water, cells were postfixed with 1% OsO_4, 1.5% potassium hexacyanoferrate(III) in water for 1 h, followed by 2% OsO_4 in water for an additional 2 h at room temperature. After brief washing in water, cells were dehydrated using a graded ethanol series in water (70% - 80% - 90% - 2 × 100%) for 10 min each. After incubation for 10 min in propylene oxide, cells were infiltrated with 30, 60, and 100% Epon in propylene oxide for 2 h each. Subsequently, cells were incubated overnight with fresh 100% Epon at room temperature. Resin was removed and Epon mixed with 1.5% accelerator (DMP-30) was added. After incubation for 2 h, samples were transferred into gelatin capsules size 00 and filled up with Epon/DMP-30. Blocks were cured at 60 °C for a minimum of 30 h and stored at room temperature. Ultrathin sections were cut using Leica Ultracut UC-7. 70 nm slices of fixed and embedded cells were transferred onto 150 mesh hexagonal copper grids coated with Pioloform. After air drying, samples were investigated without further staining.

Electrophoresis. SDS-Gel electrophoresis according to the protocol of Laemmli[39] was performed to show the binding of streptavidin and avidin to biotinylated SPION. All SPION samples that contained avidin or streptavidin were purified with Amicon 100 kDa centrifugation units three times in order to remove excess unbound streptavidin or avidin. To prove that avidin and streptavidin selectively bind to biotinylated SPION and not to PEGylated SPION without biotin, we incubated PEGylated SPION with avidin/streptavidin and subjected them to the same purification process (3 × Amicon 100 kDa) as the biotinylated SPION. All SPION were lyophilized and completely redispersed at ∼1.5 mg SPION/mL in Laemmli buffer. Clear dispersions were obtained for all SPION. All samples were split in two; one sample was denatured at 100 °C for 3 min and the other sample remained untreated. All samples were centrifuged (no pellet was observed upon centrifugation), and the supernatant was applied to a BioRad Mini-Protean TGX gradient gel (4−20% acrylamide). Separation was performed at 200 V for 45 min. Gels were stained with 0.1% Coomassie Brilliant Blue G in 40% methanol and 10% acetic acid for 15 min at 60 °C and destained with

DOI: 10.1021/acsami.6b12932
ACS Appl. Mater. Interfaces 2017, 9, 3343−3353

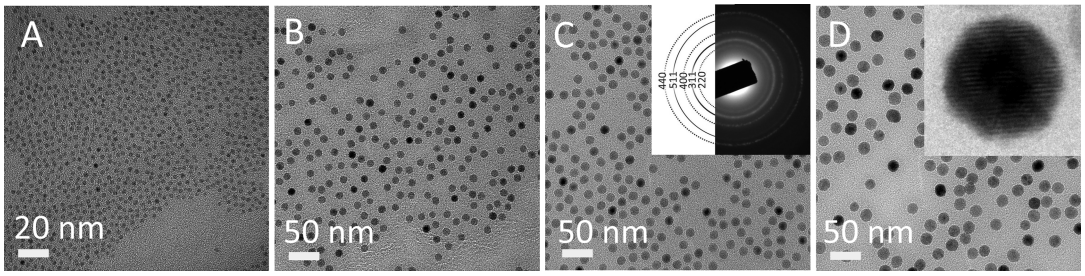

Figure 1. Transmission electron micrographs of PEGylated SPION with diameters: (A) 3.3 ± 0.3 nm, (B) 8.7 ± 0.3 nm, (C) 10.6 ± 0.4 nm, and (D) 14.4 ± 0.8 nm. The electron diffraction pattern (inset in (C)) reveals the highly crystalline nature of the SPION, and the HR-TEM inset in (D) shows that also the 14.4 nm SPION are single-crystalline.

Table 1. TGA Results for Different SPION Sizes and Coatings[a]

SPION type	ρ_{graft} [dispersant/nm^2]	TOC [%w/w]	dispersant Mw [g/mol]
3.3 nm NDA-PEG(5 kDa)	0.9	71.9	5180
8.7 nm NDA-PEG(5 kDa)	0.9	51.0	5180
8.7 nm NDA-PEG(5 kDa)-4B	1.5	62.0	5184
8.7 nm NDA-PEG(5 kDa)-90B	1.1	56.7	5256
10.6 nm NDA-PEG(5 kDa)	1.0	48.8	5180
14.4 nm NDA-PEG(5 kDa)	1.6	72.9	5180
14.4 nm NDA-PEG(10 kDa)	1.3	81.5	10180

[a]TOC was converted into grafting density, ρ_{graft}.

10% acetic acid until the background appeared colorless. Gels were scanned using a Licor Odyssey Infrared Reader.

MRI Measurements and Sample Preparation. A range of phantoms were prepared with core−shell SPION and Ferucarbotran (Resovist) in concentrations from 0.0022 to 1.79 mM_{Fe} in both Milli-Q water and 0.5% agarose to produce calibration curves by plotting the transversal relaxivities R_2 against concentration of Fe. Dispersions were filled in 1.5 mL cryo-vials and four to six of them packed into 50 mL Falcon tubes (Figure S4A). The Falcon tubes were filled bubble-free with Milli-Q water.

The phantoms were scanned at 37 °C on a Bruker Biospec 94/30 USR superconducting magnet system with a field strength of 9.4 T with a small resonator transmitter receiver coil (inner diameter = 40 mm). For T_2 relaxometry, a multi spin echo (SE) sequence with the following parameters was used: 30 different echo times (TE) with 8 ms echo spacing (TE_1 = 8 ms, TE_{30} = 240 ms), time of repetition = 2000 ms, matrix size = 256 × 256, field of view = 35 × 40 mm, 5 axial slices with a slice thickness = 1.0 mm, and a scan time of 8 min 32 s.

Postprocessing of acquired T_2 relaxometry data was done with the in-built Paravision 6.0 software. Regions of interest (ROI) were drawn manually on all axial image slices. Transversal relaxation times T_2 were calculated by exponential fitting of the signal intensity versus echo time for all ROIs separately. Mean values and standard deviations were calculated for each concentration. Relaxation rates $R_2 = 1/T_2$ were calculated and corrected by subtracting the R_2 values of the respective blanks (agarose or Milli-Q water) to give the corrected relaxation rates according to

$$R_2 = \frac{1}{T_{2,SPION\ corr}} = \frac{1}{T_{2,SPION}} - \frac{1}{T_{2,blank}} \quad (1)$$

with $T_{2,SPION}$ being the relaxation time in the presence of SPION, and $T_{2,blank}$ being the relaxation time in the absence of SPION.[40]

3. RESULTS AND DISCUSSION

SPION Analysis. About 900 as-synthesized OA-capped SPION cores were analyzed by HR- and LR-TEM for each batch using Pebbles, and the following size distributions were calculated for spherical SPION: 3.3 ± 0.3 nm, 8.7 ± 0.3 nm, 10.6 ± 0.4 nm, and 14.4 ± 0.8 nm. PEGylated SPION were purified and analyzed by HR- and LR-TEM, TGA, and DLS.

Figure 1 shows representative TEM micrographs of well-dispersed PEGylated SPION of the four sizes. The HR-TEM (inset in Figure 1D) shows the single-crystallinity of the SPION with lattice spacing in the (111) direction of 0.48 nm. The ring diffraction pattern (inset Figure 1C) reveals the highly crystalline structure of the SPION. The ratios of *d*-spacings in the obtained pattern show good agreement with the JCPDS database numbers for maghemite or magnetite.[41]

Average grafting density of PEG dispersants irreversibly bound to the surface of the SPION cores by ligand replacement was determined by TGA. The total organic content (TOC) was determined as the mass loss fraction up to 500 °C and converted into the respective dispersant grafting density using the known molecular weight of NDA-PEG(5 kDa), NDA-PEG(10 kDa), or biotinylated dispersants, the average iron oxide core area determined by TEM and a core density of 5.17 g/cm^3. Grafting densities and Mw of the respective dispersants are listed in Table 1. For mixed dispersants, such as 1.8% NDA-PEG(5 kDa)-4B or 33% NDA-PEG(5 kDa)-90B mixed with NDA-PEG(5 kDa), the Mw were calculated accordingly.

SPION Relaxivity. The efficiency of SPION as contrast agents can be described by their relaxivity, which is related to the reciprocal transverse relaxation time $1/T_{2,SPION}$ and the concentration of the SPION. The relaxivity was obtained by measuring the transversal relaxation times at different SPION concentrations and plotting the corrected relaxation rates R_2 (i.e., the inverse relaxation times $1/T_{2,SPION\ corr}$) according to eq 1 against Fe concentration. By using corrected inverse relaxation times, the relaxivity R_2 [mM_{Fe}^{-1} s^{-1}] is the slope of a linear fit to the relaxation rates as a function of Fe concentration, and can be directly read from the *y*-axis at a Fe concentration of 1 mM.

We investigated the dependence of the R_2 relaxivity, which is most commonly used for imaging with SPION as negative CA, on the SPION core size. The relaxivity of four core diameters were directly compared: 3.3, 8.7, 10.6, and 14.4 nm. This is only possible due to the uniquely monodisperse synthesis and

DOI: 10.1021/acsami.6b12932
ACS Appl. Mater. Interfaces 2017, 9, 3343−3353

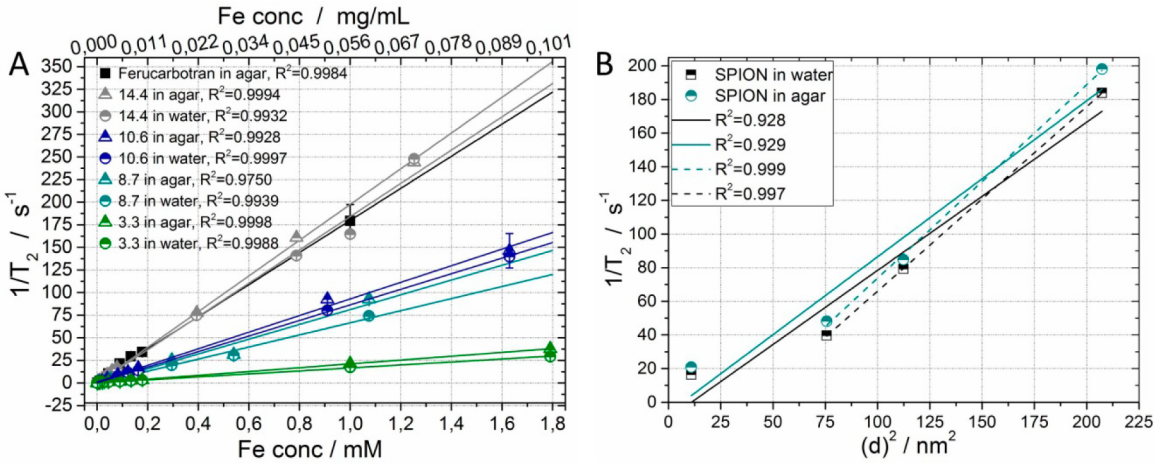

Figure 2. (A) Corrected transversal relaxation rates $1/T_2$ as a function of Fe concentration measured in a 9.4 T field. SPION were dispersed in H_2O (circles) or agarose (triangles). Different diameters of core−shell SPION (3.3 nm - green, 8.7 nm - cyan, 10.6 nm - dark blue, 14.4 nm - gray) were compared to Ferucarbotran (Resovist) (black squares). All SPION are coated with NDA-PEG(5 kDa). The linear regression fits in water all had $R^2 > 0.99$. (B) Corrected transversal relaxivity R_2 at 1 mM_{Fe} as a function of d^2. R_2 shows a near perfect linear scaling with d^2 when the 3.3 nm SPION are excluded. The linear regression fit in water had $R^2 > 0.99$.

Table 2. Relaxivities R_2 at 1 mM_{Fe} for Different Diameters of Individual PEG-Stabilized Core−Shell SPION and Ferucarbotran Measured at 9.4 T and Literature Values for R_2 Relaxivities of Benchmark Contrast Agents Measured at 1.5 or 3 T[25]

SPION type	R_2 [mM_{Fe}^{-1} s^{-1}] in Milli-Q	R_2 [mM_{Fe}^{-1} s^{-1}] in agarose	$R_{2\ norm}$ [mM_{Fe}^{-1} s^{-1}] in Milli-Q	$R_{2\ norm}$ [mM_{Fe}^{-1} s^{-1}] in agarose
Ferucarbotran		179/186[a]		
Ferumoxid		120[a]		
Ferumoxtran-10		65[a]		
PEGylated SPION, 3.3 nm	16.4	20.9	1.5	1.9
PEGylated SPION, 8.7 nm	39.6	48.1	0.5	0.6
PEGylated SPION, 10.6 nm	79.2	84.8	0.7	0.8
PEGylated SPION, 14.4 nm	183.9	198.1	0.9	1.0

[a]Literature values.

individual stabilization of the NDA-PEG-grafted SPION. Figure 2A shows the corrected transversal relaxation rate $1/T_{2,SPION\ corr}$ as a function of iron concentration and thereby the relaxivities R_2 for the different SPION compared to Ferucarbotran SPION (Resovist) as benchmark.

As expected, the relaxation rates of all SPION increase linearly with Fe concentration. The transversal relaxivity R_2 increases with increasing SPION core size. A larger single-crystal core size is expected to correspond to a higher magnetic moment per core, but it also changes the diffusion time within the zone around a particle within which dephasing can occur. A comparison of relaxivities expressed in mM_{Fe}^{-1} s^{-1} of our core−shell SPION to the literature and measured values is given in Table 2.

An efficient MRI contrast agent features the ability to shorten the relaxation time T_2 of surrounding water protons effectively, i.e., to increase the loss in phase coherence of the transverse magnetization of the water protons in the vicinity of the contrast agent. The magnetic susceptibility of the superparamagnetic contrast agent causes disturbances in the local magnetic field, which leads to an increased exchange of energy between spins, an increased loss of transverse phase coherence, and finally to a faster decline of the transverse magnetization. High relaxivity, $R_2 = 1/T_2$, is influenced by various factors, by the magnetic moment of the core, SPION concentration, temperature, diffusion coefficient of water (protons) within the dephasing region in the vicinity of the core, magnetic field strength and radiofrequency that is applied, the number of water molecules within the distorted field of the SPION, the distance between the SPION and the protons of the water molecules, and the dynamic exchange of those water molecules within the field of the particle with bulk water molecules.[40,42] In short, the dominating contributions to increasing the relaxivity that can be influenced by design of the SPION is a large core size (high magnetic moment and large dephasing zone) and close proximity of a large amount of water protons that diffuse slowly in the vicinity of the SPION core.

For strongly magnetized, small nanoparticles, the relaxation rate is supposedly given by the quantum mechanical outer sphere theory, for which motional averaging can be assumed such that the relaxation is not interrupted by refocusing echo-pulses.[43] In this regime, R_2 is linearly related to the volume fraction (concentration) of magnetic spheres and also scaling with the diameter d, as d^2. This small SPION size range is for iron oxide cores expected to be $d < 35$ nm.[42] The dependence on nanoparticle size is predominantly a consequence of the scaling of the diffusion timescale

$$\tau_D = d^2/D \tag{2}$$

where D is the diffusion coefficient of the protons.[44] Thus, the main size dependence is not expected from the magnetic properties of the core. Except for the cores with a diameter of 3.3 nm, the scaling expected from eq 2 is well observed (Figure 2B), but with a marginally increasing trend in size-normalized relaxivity with core size (Table 2).

DOI: 10.1021/acsami.6b12932
ACS Appl. Mater. Interfaces 2017, 9, 3343−3353

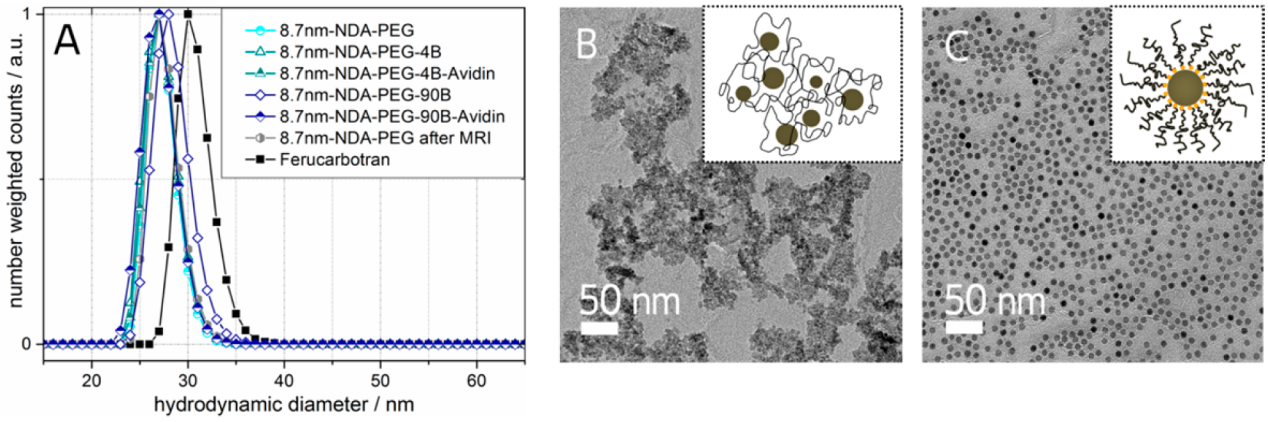

Figure 3. (A) DLS hydrodynamic diameter size distributions of 8.7 nm core−shell SPION with different coatings before MRI measurements, 8.7 nm PEGylated SPION after MRI measurements, and Ferucarbotran. Representative DLS autocorrelation functions are shown in Figure S7. (B) TEM micrograph of drop-casted Ferucarbotran and (C) 8.7 nm PEGylated core−shell NPs. The insets depict sketches of the NP preparations. Ferucarbotran has multiple cores distributed in a physisorbed carboxydextran matrix, whereas SPION in (C) have an individual covalently grafted PEG shell.

Table 3. Average Hydrodynamic Diameters (D_H) for the Number-Weighted Size Distribution of Differently Functionalized Core−Shell SPION and Polydispersity Indices (PDI) for the Fitted Distributions

	D_H [nm]	mean PDI [a.u.]	PDI standard deviation [%]
PEG(5 kDa)	15.8	0.27	4.0
8.7 nm-PEG	26.9	0.19	0.6
8.7 nm-PEG after MRI	27.0	0.23	0.2
8.7 nm-NDA-PEG-4B	27.0	0.18	0.2
8.7 nm-NDA-PEG-4B-Avidin	27.3	0.29	0.8
8.7 nm-NDA-PEG-90B	27.9	0.23	1.0
8.7 nm-NDA-PEG-90B-Avidin	27.2	0.33	0.5
Resovist	30.8	0.19	1.0

As the cores increase in size, the curvature of the surface decreases. Additionally, the largest cores also have the highest grafting density. These two factors will both contribute to a thicker and denser polymer brush. The volume of water interacting with the dense PEG brush in the vicinity of the core is, therefore, increasing for these three sizes and thereby provides a larger number of water protons with reduced diffusion coefficient as the core size is increased; this will lead to higher relaxivity as observed from eq 2.[42,45] An additional explanation can be the lower core volume fraction of the demagnetized layer at the surface of the nanoparticles created by the nitrocatechol-anchored PEG as core size is increased;[46,47] this reduces the core magnetic moment, but relatively less so the larger the core is.

In this context, one can note that the relaxivity curve has an intercept at nonzero diameter. This seems to indicate that there is a part of the nanoparticle that does not contribute to the magnetic moment, and that this contribution has a similar size dependence as the diffusion time constant. For example, nanoparticle crystallinity is compromised through the surface distortion and chelation of ligands such that a part of the particle does not contribute to the magnetic moment.[46]

During particle growth, other crystal defects such as twinning can also occur.[48] At $d \approx 6$ nm, the extrapolation of R_2 of the larger nanoparticles yields $R_2 = 0$; this implies that no magnetic distortion of the proton relaxation should be present below this size. However, we observe that our smallest nanoparticles with a diameter of 3.3 nm have a non-negligible relaxivity that is significantly higher than the trend. Since it is difficult to explain from physical considerations, the outlier presented by the 3.3 nm cores could be due to the larger polydispersity in size and shape of the cores as well as the potentially larger systematic measurement error of small particles due to lower contrast and resolution limitation. It is also possible that the magnetic core size strongly deviates from the geometrical core size used to plot Figure 2B, as shown by Luigjes et al.[48] They concluded that crystal defects play a larger role to determine the nanoparticle magnetic properties than the size. Highly uniform, especially spherical, iron oxide nanoparticles have a much broader distribution of defects; therefore, their distribution of effective magnetic core size is much broader than the polydispersity in the geometric size distribution implies. Without additional data to characterize the magnetic core size distribution, we can only observe that the expected scaling with geometric size for larger particles implies that at least the relationship between the magnetic core size and the physical core size is similar for different sizes. Luigjes et al. observed that less spherical, faceted (annealed) and smaller (slower grown) iron oxide nanoparticles have relatively larger magnetic core sizes in closer agreement with their geometric size. Although the uniformity of the 3.3 nm cores is much lower than that for the larger cores, they are faceted rather than spherical and could, therefore, have a stronger dipole moment relative to their size compared to the larger particles. This could help explain their higher relaxivity than predicted by the extrapolation of the values for larger particles. It should also be noted that the estimate obtained by extrapolating the highly spherical large-core SPION yields an unrealistically high diameter at which the magnetization should be negligible.

DOI: 10.1021/acsami.6b12932
ACS Appl. Mater. Interfaces 2017, 9, 3343−3353

Finally, we observe that the 14.4 nm PEGylated SPION demonstrate an R_2-relaxivity higher than every benchmark SPION contrast agent found in the literature.[3,25,49] The strong dependence of R_2 on size leads to a lower relaxivity for our smaller core sizes than the best previously published single-core contrast agents.[25,50,51] The high performance of the 14.4 nm PEGylated SPION is likely due to that they largely meet the design criteria described above for optimizing relaxivity by having a large core size and dense PEG shell. In combination with perfect colloidal stability in the 9.4 T magnetic field, they indeed show excellent performance and flexibility on all key performance criteria.

A striking difference in the aggregation state is observed in the TEM micrographs in Figure 3B,C between Ferucarbotran, which is stabilized by physisorbed carboxydextran, and core−shell SPION stabilized by irreversibly grafted PEG. Micrographs and cartoons (insets in Figure 3B,C) illustrate the matrix-like nature of Ferucarbotran drop-casted on the TEM grid in contrast to the individually stabilized core−shell SPION. However, the DLS data (Figure 3A and Table 3) indicate a similar size distribution of around 26−28 nm in hydrodynamic diameter (D_H) for all types of core−shell SPION.

D_H measured for core−shell SPION are in good agreement with literature values for individually stabilized core−shell SPION.[20,52,53] The measured D_H coincide well with earlier findings for SPION densely grafted with NDA-PEG that were investigated by small-angle X-ray scattering.[54] The thickness of the dense part of the PEG shell was for smaller cores fitted to be 6.4 nm. Adding this thickness to a SPION core size of 8.7 nm gives a core−shell SPION diameter of 21.5 nm. This is in very good agreement with our D_H measurements considering the uncertainty of the measurement methods and that the hydrodynamic diameter will be sensitive to the diffuse tail region, which was not taken into account in the previous study. Alternatively, one can compare the core−shell D_H to the D_H obtained for free PEG(5 kDa), which was measured to be 15.8 nm (Figure S8). Adding the free coil size as a shell to a SPION core size of 8.7 nm sums up to a D_H of ∼40 nm. This seems to be an overestimation of the actual size of the core−shell nanoparticles. These measurements, as well as TEM images (Figure 1 and 3C) and the low polydispersity indices (Table 3), strongly support that the SPION have an individual core−shell structure and that clustering (e.g., multiple cores with one grafted shell) is highly improbable. The hydrodynamic diameter measured for Ferucarbotran (31 nm) was slightly higher than that for core−shell SPION (Figure 3A and Table 3). It should be noted that the hydrodynamic diameter measured for particles coated by physisorbed polymer is likely to be sensitive to the measurement conditions and sample history. Typical literature values reported for Ferucarbotran are 45−60 nm,[19,25] and thus substantially larger than the ∼31 nm measured here. As evident from our data, high relaxivities can be achieved by either increasing the geometric and magnetic (moment) core size or by core clustering, as in the example of Ferucarbotran. To our knowledge, the relaxivity reported for our 14.4 nm SPION is the highest relaxivity ever reported for individually stabilized core−shell nanoparticles; it is even higher than that of the cluster-core Ferucarbotran.[55]

Ferucarbotran SPION are in general considered to be colloidally stable in conditions such as low protein concentration at room temperature. However, the colloidal stability reaches its limits when these CAs are applied in biologically relevant conditions as shown earlier.[27] Although having a comparable hydrodynamic diameter and comparable polydispersity index measured by DLS (Table 3), the advantage of the core−shell architecture over the physisorbed Ferucarbotran matrix-like structure became obvious during the relaxivity measurements. While the relaxivity of core−shell SPION could be measured in pure water without fixation even for MRI fields of 9.4 T, Ferucarbotran SPION had to be fixed in an agarose matrix in order to not immediately aggregate and precipitate in the strong magnetic field. DLS measurements of PEGylated SPION after MRI (Figure 3A) confirmed that no aggregation had occurred and the hydrodynamic diameter did not change along with only a slight increase of the PDI (Table 3). Interestingly, the measured relaxivities of SPION were always found to be higher in agarose. The presence of agarose reduces the diffusion coefficient of water, which increases the residence time of protons within the dephasing magnetic field of the SPION. The relative difference in diffusion coefficient between water within a hydrophilic matrix close to the SPION and free water determines the magnitude of the increase in relaxivity, as seen from eq 2. A large difference in the diffusion coefficient can, therefore, theoretically lead to a large difference in relaxivity, and it has been shown to practically lead to up to a factor of 2 increase in relaxivity for small SPION.[42] A similar effect was also experimentally verified by Paquet et al. for clusters of SPION enwrapped in hydrogel.[45] The comparison of relaxivities for SPION that have to be fixed in agarose, which to the best of our knowledge is the norm applied to all such comparisons of second and third generation contrast agents to date, thus overstates the actual obtainable relaxivity for most SPION.

It has been shown that the induced dephasing and, therefore, the relaxivity change introduced by aggregates of nanoparticles can be effectively modeled by a magnetic nanoparticle of similar core size. Our results show that, although Ferucarbotranes and similar enwrapped multicore SPION combine attractive features for high relaxivity such as core aggregation, high water volume in close proximity to the magnetic core and a diffusion-retarding hydrophilic polymer matrix, the combined effect of these contributions is inferior to optimizing the size and coating of an individual core. Other reported record relaxivities, such as those by Maity et al.[56] and other second generation contrast agents, by Paquet et al.[45] for hydrogel-enwrapped SPION clusters, or by Weller et al.[55] for nanoclusters of NPs, are explained by strong unintended or intended aggregation, as evidenced by the TEM and DLS data. High relaxation times for core−shell SPION have also been reported by Wang et al.,[50] although here the TEM micrographs and the relatively high D_H strongly suggest the enwrappment of multiple cores into one shell, leading to a higher relaxivity.

The aggregation of insufficiently stabilized or macromolecularly bridged nanoparticle contrast agents might seem like a viable way to increase relaxivity and performance as contrast agent. However, the resulting larger size and much stronger nonspecific colloidal interactions compromise the ability to perform biomolecule-mediated targeting.[12] This is demonstrated by the inability to measure relaxivities in water as well as by the cell uptake measurements presented below.

Qualitative Electrophoretic Analysis of Streptavidin- and Avidin-Functionalized SPION. Nonspecific adsorption of proteins to insufficiently stabilized nanoparticles is often an issue. Therefore, we compared the adsorption of streptavidin and avidin to PEGylated SPION with and without biotin functionalization (PEG-SPION with 90 biotin/SPION). We

DOI: 10.1021/acsami.6b12932
ACS Appl. Mater. Interfaces 2017, 9, 3343−3353

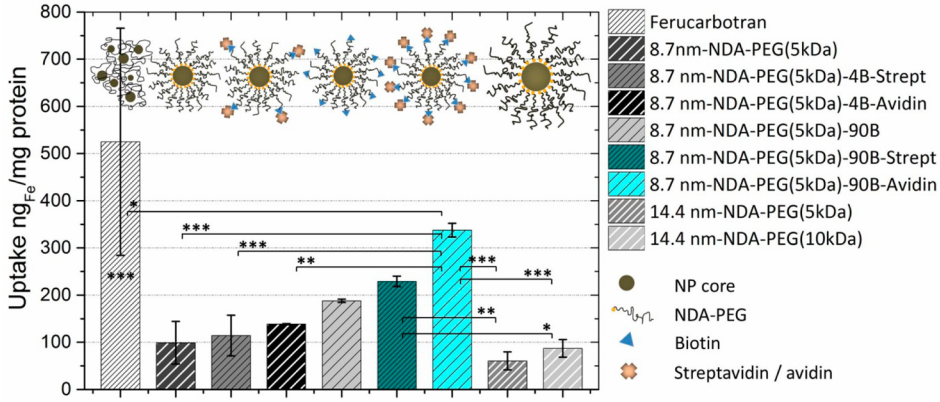

Figure 4. Macrophage uptake of different core−shell SPION architectures compared to Ferucarbotran. Cells were incubated with the respective SPION dispersions for 20 h, and the intracellular Fe content was measured by a Ferrozine assay. At least 3 independent experiments with 3 wells/experiment were performed for each data point. Statistical analysis was done by 1-way ANOVA test. ***$p < 0.001$, **$p < 0.01$, *$p < 0.05$. Ferucarbotran was taken up more than any of the core−shell preparations with high statistical significance (***$p < 0.001$), except for 8.7 nm-NDA-PEG-90B-Avidin (*$p < 0.05$), as indicated in the graph.

found, in accordance with previous results,[27] that nonspecific binding of protein to the PEGylated SPION is negligible (Figures S5 and S6). In contrast, when proteins were specifically coupled via the strong biotin−avidin/streptavidin bond, all protein was detected on the SPION and colored the SPION band on the gel upon Coomassie staining. When the samples were denatured at 100 °C in SDS, a prominent band at 15 kDa appeared, representing the denatured, monomeric protein released from the SPION.

Cellular Uptake. Cell uptake by insufficiently camouflaged nanoparticles is an uncontrolled problem in most testing and application of biomedical nanoparticles. It is driven by nonspecific interactions with protein and membranes, and it is a bottleneck in drug delivery due to opsonization and phagocytosis performed by macrophages that clear nanoparticles from the blood. To demonstrate the potential of individually stabilized PEGylated core−shell SPION to evade RES clearance, we investigated their uptake by macrophages for two core sizes (8.7 and 14.4 nm in diameter) and different surface modifications: pure PEGylated SPION, SPION with low and high biotin density in the shell as well as SPION coated by streptavidin or avidin. The large core sizes were chosen for the uptake experiments because of their superior performance in MRI measurements compared to the smaller core sizes. Ferucarbotran, which are carboxydextran-coated SPION, were chosen as control and benchmark. The amounts of SPION taken up by macrophages are shown in Figure 4, quantified as average ng$_{Fe}$/mg cell protein content adjusted for the amount in control cells that were not exposed to SPION. Values were calculated from 3 up to 7 individual uptake experiments and at least 3 individual wells per type of SPION.

Both PEGylated 8.7 and 14.4 nm SPION showed negligible uptake of around 100 ng Fe/mg protein. We did not find a significant difference in the uptake of SPION grafted with the same density of PEG(5 kDa) and PEG(10 kDa), respectively. This contrasts a previous study by Leal et al.[57] in which SPION were grafted with gallol-PEG of different Mw, but with very different grafting densities (0.3−1.6 molecules/nm^2). The low affinity anchor[29] and the different grafting densities rather than the different PEG molecular weights could thus have led to the observed differences in uptake in their study. In line with our results, Park et al. reported a similar uptake rate for SPION stabilized with PEG of different molecular weights.[58] However, in their study, a negligible uptake after 1 h incubation of cells with SPION was reported. After 5 h, an immense uptake had taken place, which is in stark contrast to our results in which negligible uptake was observed even after 20 h. In the study by Park et al., low affinity anchors such as carboxylic groups were applied that do not ensure sufficient colloidal stability under the conditions of cell culture with competing adsorbing species in solution.[29] Thus, high cellular uptake can be expected after relatively short incubation times due to aggregation.

It is striking that our individually stabilized, PEGylated core−shell SPION are 5 times less likely to be eaten by cells than Ferucarbotran. The latter also showed a huge variability in cell uptake experiments compared to PEGylated SPION (see error bar in Figure 4), which is a consequence of its tendency to aggregate in the growth medium. The aggregation and uneven uptake by macrophages are caused by insufficient colloidal stability at high salt and protein concentrations that reduces the steric stabilization provided by physisorbed polymers such as carboxydextran. In contrast, we have previously demonstrated negligible protein and membrane interactions of densely grafted PEGylated core−shell SPION,[27] which translated into low uptake by HeLa and HEK cell lines.[27,59] Obviously, the small uniform size and successful suppression of nonspecific interactions with biomolecules also translates into the low nonspecific uptake by macrophages demonstrated in Figure 4. Avoiding nonspecific and specific pinocytosis and phagocytosis by phagocytic cells is an even more daunting feat than low uptake by cancer cell lines. Compared to Gal et al.,[59] the difference in uptake between Ferucarbotran and PEGylated core−shell nanoparticle uptake is even larger for phagocytic cells than for standard cell lines.

To further demonstrate the influence of protein adsorption at the nanoparticle surface on active cell uptake, we prepared SPION with on average 4 biotin-functionalized PEG per SPION as well as SPION with on average 90 PEG-biotin per SPION. Streptavidin and avidin were specifically coupled to the PEG-shell of the SPION using the biotin linker. As can be seen in Figure 4, four biotin-streptavidin units are not enough to significantly increase uptake of SPION. The uptake increased about a factor of 2 in comparison to only PEGylated SPION when a high fraction of biotinylated NDA-PEG was grafted. It is notable that the addition of biotin-functionalized PEG (90 biotin/SPION) led to a significant increase in uptake, while

DOI: 10.1021/acsami.6b12932
ACS Appl. Mater. Interfaces 2017, 9, 3343−3353

further functionalization of such particles with streptavidin led to no increase in uptake compared to PEGylated particles without functionalization. This indicates that already the presence of a high surface density of the small functional molecular group biotin is sufficient to cause nonspecific protein interactions, leading to increased cell uptake. Streptavidin is known to have low nonspecific binding due to the absence of glycosylation and is a frequently used building block for biomolecular coupling in biotechnology using biotinylated proteins, e.g., antibodies, and, therefore, serves to mask the biotin interaction. It is also notable that SPION decorated with just a few streptavidin are not more likely to be taken up than purely PEGylated SPION. Even SPION that are potentially fully coated by streptavidin demonstrate cell internalization that is less than half of that of Ferucarbotran and with very low variability. This points to aggregation of nanoparticles and increased average size as significant drivers for cell uptake, potentially by promoting phagocytosis.

Streptavidin's homologue avidin has higher affinity for biotin, but is additionally glycosylated, leading to a positive surface charge at physiological pH.[60] Coupling of avidin instead of streptavidin led to near 4-fold increased uptake compared to PEGylated SPION and 2-fold increase compared to PEGylated SPION with biotin functionalization. Positively charged proteins are more likely to be taken up by endocytosis due to their high affinity to negatively charged cell surfaces.[61,62]

In fact, all core−shell SPION, irrespective of surface coating, were significantly less taken up than the benchmark contrast agent. These results demonstrate the potential to circumvent the problem of nonspecific interactions preventing specific targeting observed for first generation SPION contrast agents. A dense PEG-shell of sufficient thickness suppresses nonspecific interactions, and biotinylated ligands can be attached to the SPION with a low number of biotin-streptavidin linkers.[51]

TEM Observations of Cellular Uptake. Nanoparticles interacting nonspecifically with cells are expected to be taken up through the endosome and degraded in lysosomes. Active phagocytosis or pinocytosis of SPION that are not sufficiently shielded from nonspecific or specific recognition is, therefore, expected to lead to a large presence of SPION in the endosome and lysosome, in which they are then degraded. Noninteracting stealth SPION could still be taken up through the act of nonspecific cell drinking (pinocytosis), by which the SPION is transported as part of the internalized extra-cellular liquid, at the high SPION concentration that macrophages are subjected to in our uptake experiments. We, therefore, prepared thin sections of macrophages to localize the position of SPION taken up by macrophages.

Figure 5 shows representative transmission electron micrographs of macrophages washed and fixed after 20 h incubation with Ferucarbotran or PEGylated core−shell SPION. Macrophages incubated with Ferucarbotran showed several stages of endocytic uptake (Figure 5A). Red arrows indicate positions of nanoparticles. SPION were not detected in endosomes in any of the thin sections of macrophages incubated with PEGylated core−shell SPION (8.7 nm, either PEGylated, PEG-90B-Avidin, or PEG-4B-Strept). TEM is not a quantitative or statistical method to evaluate cell uptake. However, the absence of core−shell SPION in any thin section points to that their uptake was too low to be reliably detected with this method. The vast difference between Ferucarbotran SPION and PEG-grafted core−shell SPION indicates that the latter largely evade macrophage uptake (only taken up by cell drinking) and is in line with the results of the iron quantification by Ferrozine testing.

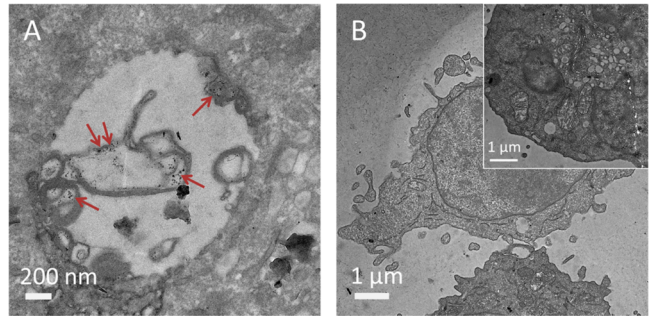

Figure 5. TEM micrographs of thin sections of macrophages incubated for 20 h with SPION. (A) Macrophages incubated with Ferucarbotran. The red arrows indicate an abundance of SPION incorporated in the endosome. (B) Macrophages incubated with PEGylated core−shell SPION (8.7 nm): no core−shell SPION could be found in endosomes in a large number of investigated cells. Pictures shown are representative for >20 cells in different thin sections that were examined.

4. CONCLUSION

We could for the first time demonstrate the measurement of transversal relaxivity R_2 for densely PEG-grafted core−shell SPION in water without stabilization in an agarose matrix even at a magnetic field strength of 9.4 T. This highlights the exceptional colloidal stability already reported for this type of SPION,[27,59] and which here was shown to translate also into remarkably low uptake by phagocytic cells of the RES. We conclude that careful design of core−shell SPION with precise synthetic control over core size and irreversibly grafted, dense shell composition leads to superior stability in biological media, under the influence of strong magnetic fields and most importantly in the presence of macrophages and other phagocytic cells. Such biocompatible iron oxide SPION showing negligible uptake by macrophages even when functionalized with protein ligands hold the promise to be a new generation of SPION contrast agents used for targeted MRI. Furthermore, by choosing ligands tethered to the PEG-shell, in this case, the cationic glycosylated protein avidin, cell uptake could be stimulated for originally stealth SPION.

The combination of stealth capability *in vitro* and very high relaxivity for small overall nanoparticle size is likely to translate into the possibility to use drastically lower injected amounts of SPION for MRI and related applications. This will lower toxicity issues and the load on organs responsible for clearing nanomaterials in the body. We emphasize that, while high relaxivities can be observed for multicore SPION and low cell uptake can be observed for small core−shell SPION, the combination of these properties was only observed for large, monodisperse, single-crystalline iron oxide cores that are individually stabilized with a densely and irreversibly grafted polymer shell that suppresses nonspecific interactions. We have also demonstrated that these SPION can be produced in large amounts and be used as a platform to create a set of differently functionalized and targeted contrast agents.

■ ASSOCIATED CONTENT

Supporting Information

The Supporting Information is available free of charge on the ACS Publications website at DOI: 10.1021/acsami.6b12932.

DOI: 10.1021/acsami.6b12932
ACS Appl. Mater. Interfaces 2017, 9, 3343−3353

Additional synthesis information and characterization of chemical compounds, DLS data, and detailed description of electrophoresis and phantom samples (PDF)

AUTHOR INFORMATION

Corresponding Author

*E-mail: Erik.reimhult@boku.ac.at.

ORCID

Erik Reimhult: 0000-0003-1417-5576

Author Contributions

The study was planned by E. Reimhult, T. Helbich, and A. Lassenberger. Cell culture and Ferrozine assays were done by A. Scheberl. A. Lassenberger prepared all NP samples and performed most measurements. A. Stadlbauer developed the MRI sequence and A. Stiglbauer performed the MRI measurements. The manuscript was written by A. Lassenberger and E. Reimhult. All authors have given approval to the final version of the manuscript.

Funding

The research leading to these results received funding from the European Research Council under the European Union's Seventh Framework Programme (FP/2007-2013)/ERC Grant Agreement no. 310034.

Notes

The authors declare no competing financial interest.

ACKNOWLEDGMENTS

We thank Lubos Budinsky for support with the MRI measurements. We thank Tanja Zwölfer for support in the NP synthesis.

REFERENCES

(1) Wang, Y.-X. J. Superparamagnetic Iron Oxide Based Mri Contrast Agents: Current Status of Clinical Application. *Quant. Imaging Med. Surg.* **2011**, *1*, 35−40.

(2) Liu, G.; Gao, J.; Ai, H.; Chen, X. Applications and Potential Toxicity of Magnetic Iron Oxide Nanoparticles. *Small* **2013**, *9*, 1533−1545.

(3) Ling, D.; Hyeon, T. Iron Oxide Nanoparticles: Chemical Design of Biocompatible Iron Oxide Nanoparticles for Medical Applications. *Small* **2013**, *9*, 1450−1466.

(4) Bixner, O.; Lassenberger, A.; Baurecht, D.; Reimhult, E. Complete Exchange of the Hydrophobic Dispersant Shell on Monodisperse Superparamagnetic Iron Oxide Nanoparticles. *Langmuir* **2015**, *31*, 9198−9204.

(5) Corot, C.; Robert, P.; Idee, J.-M.; Port, M. Recent Advances in Iron Oxide Nanocrystal Technology for Medical Imaging. *Adv. Drug Delivery Rev.* **2006**, *58*, 1471−1504.

(6) Corot, C.; Warlin, D. Superparamagnetic Iron Oxide Nanoparticles for MRI: Contrast Media Pharmaceutical Company R&D Perspective. *Wiley Interdiscip. Rev.: Nanomed. Nanobiotechnol.* **2013**, *5*, 411−422.

(7) Memarsadeghi, M.; Riedl, C. C.; Kaneider, A.; Galid, A.; Rudas, M.; Matzek, W.; Helbich, T. H. Axillary Lymph Node Metastases in Patients with Breast Carcinomas: Assessment with Nonenhanced Versus Uspio-Enhanced MR Imaging. *Radiology* **2006**, *241*, 367−377.

(8) *Withdrawal Assessment Report for Sinerem*; European Medicines Agency: London, 2008.

(9) Heesakkers, R. A. M.; Jager, G. J.; Hovels, A. M.; de Hoop, B.; van den Bosch, H. C. M.; Raat, F.; Witjes, J. A.; Mulders, P. F. A.; van der Kaa, C. H.; Barentsz, J. O. Prostate Cancer: Detection of Lymph Node Metastases Outside the Routine Surgical Area with Ferumoxtran-10-Enhanced Mr Imaging. *Radiology* **2009**, *251*, 408−414.

(10) Wang, Y.-X. J. Current Status of Superparamagnetic Iron Oxide Contrast Agents for Liver Magnetic Resonance Imaging. *World J. Gastroenterol.* **2015**, *21*, 13400−13402.

(11) Reddy, L. H.; Arias, J. L.; Nicolas, J.; Couvreur, P. Magnetic Nanoparticles: Design and Characterization, Toxicity and Biocompatibility, Pharmaceutical and Biomedical Applications. *Chem. Rev.* **2012**, *112*, 5818−5878.

(12) Stephen, Z. R.; Kievit, F. M.; Zhang, M. Magnetite Nanoparticles for Medical MR Imaging. *Mater. Today* **2011**, *14*, 330−338.

(13) Wang, Y. X.; Hussain, S. M.; Krestin, G. P. Superparamagnetic Iron Oxide Contrast Agents: Physicochemical Characteristics and Applications in MR Imaging. *Eur. Radiol.* **2001**, *11*, 2319−2331.

(14) Hamm, B.; Staks, T.; Taupitz, M.; Maibauer, R.; Speidel, A.; Huppertz, A.; Frenzel, T.; Lawaczeck, R.; Wolf, K. J.; Lange, L. Contrast-Enhanced MR Imaging of Liver and Spleen: First Experience in Humans with a New Superparamagnetic Iron Oxide. *J. Magn. Reson. Imaging* **1994**, *4*, 659−668.

(15) Thorek, D. L. J.; Chen, A. K.; Czupryna, J.; Tsourkas, A. Superparamagnetic Iron Oxide Nanoparticle Probes for Molecular Imaging. *Ann. Biomed. Eng.* **2006**, *34*, 23−38.

(16) Byrne, J. D.; Betancourt, T.; Brannon-Peppas, L. Active Targeting Schemes for Nanoparticle Systems in Cancer Therapeutics. *Adv. Drug Delivery Rev.* **2008**, *60*, 1615−1626.

(17) Lacava, L. M.; Lacava, Z. G. M.; Da Silva, M. F.; Silva, O.; Chaves, S. B.; Azevedo, R. B.; Pelegrini, F.; Gansau, C.; Buske, N.; Sabolovic, D.; Morais, P. C. Magnetic Resonance of a Dextran-Coated Magnetic Fluid Intravenously Administered in Mice. *Biophys. J.* **2001**, *80*, 2483−2486.

(18) Hong, R. Y.; Feng, B.; Chen, L. L.; Liu, G. H.; Li, H. Z.; Zheng, Y.; Wei, D. G. Synthesis, Characterization and MRI Application of Dextran-Coated Fe3O4Magnetic Nanoparticles. *Biochem. Eng. J.* **2008**, *42*, 290−300.

(19) Reimer, P.; Balzer, T. Ferucarbotran (Resovist): A New Clinically Approved Res-Specific Contrast Agent for Contrast-Enhanced MRI of the Liver: Properties, Clinical Development, and Applications. *Eur. Radiol.* **2003**, *13*, 1266−1276.

(20) Amstad, E.; Textor, M.; Reimhult, E. Stabilization and Functionalization of Iron Oxide Nanoparticles for Biomedical Applications. *Nanoscale* **2011**, *3*, 2819−2843.

(21) Stone, R. C.; Qi, B.; Trebatoski, D.; Jetti, R.; Bandera, Y. P.; Foulger, S. H.; Mefford, O. T. A Versatile Stable Platform for Multifunctional Applications: Synthesis of a Nitrodopa-PEO-Alkyne Scaffold for Iron Oxide Nanoparticles. *J. Mater. Chem. B* **2014**, *2*, 4789−4793.

(22) Lak, A.; Dieckhoff, J.; Ludwig, F.; Scholtyssek, J. M.; Goldmann, O.; Luensdorf, H.; Eberbeck, D.; Kornowski, A.; Kraken, M.; Litterst, F. J.; Fiege, K.; Mischnick, P.; Schilling, M. Highly Stable Monodisperse Pegylated Iron Oxide Nanoparticle Aqueous Suspensions: A Nontoxic Tracer for Homogeneous Magnetic Bioassays. *Nanoscale* **2013**, *5*, 11447−11455.

(23) Wei, H.; Insin, N.; Lee, J.; Han, H.-S.; Cordero, J. M.; Liu, W.; Bawendi, M. G. Compact Zwitterion-Coated Iron Oxide Nanoparticles for Biological Applications. *Nano Lett.* **2012**, *12*, 22−25.

(24) Wang, W.; Ji, X.; Na, H. B.; Safi, M.; Smith, A.; Palui, G.; Perez, J. M.; Mattoussi, H. Design of a Multi-Dopamine-Modified Polymer Ligand Optimally Suited for Interfacing Magnetic Nanoparticles with Biological Systems. *Langmuir* **2014**, *30*, 6197−6208.

(25) Na, H. B.; Song, I. C.; Hyeon, T. Inorganic Nanoparticles for MRI Contrast Agents. *Adv. Mater.* **2009**, *21*, 2133−2148.

(26) Ling, D.; Hyeon, T. Chemical Design of Biocompatible Iron Oxide Nanoparticles for Medical Applications. *Small* **2013**, *9*, 1450−1466.

(27) Lassenberger, A.; Bixner, O.; Gruenewald, T.; Lichtenegger, H.; Zirbs, R.; Reimhult, E. Evaluation of High-Yield Purification Methods on Monodisperse Peg-Grafted Iron Oxide Nanoparticles. *Langmuir* **2016**, *32*, 4259−4269.

(28) Zirbs, R.; Lassenberger, A.; Vonderhaid, I.; Kurzhals, S.; Reimhult, E. Melt-Grafting for the Synthesis of Core-Shell Nano-

DOI: 10.1021/acsami.6b12932
ACS Appl. Mater. Interfaces 2017, 9, 3343−3353

particles with Ultra-High Dispersant Density. *Nanoscale* **2015**, *7*, 11216−11225.
(29) Amstad, E.; Gillich, T.; Bilecka, I.; Textor, M.; Reimhult, E. Ultrastable Iron Oxide Nanoparticle Colloidal Suspensions Using Dispersants with Catechol-Derived Anchor Groups. *Nano Lett.* **2009**, *9*, 4042−4048.
(30) Bae, J.-E.; Huh, M.-I.; Ryu, B.-K.; Do, J.-Y.; Jin, S.-U.; Moon, M.-J.; Jung, J.-C.; Chang, Y.; Kim, E.; Chi, S.-G.; Lee, G.-H.; Chae, K.-S. The Effect of Static Magnetic Fields on the Aggregation and Cytotoxicity of Magnetic Nanoparticles. *Biomaterials* **2011**, *32*, 9401−9414.
(31) Mondini, S.; Ferretti, A. M.; Puglisi, A.; Ponti, A. Pebbles and Pebblejuggler: Software for Accurate, Unbiased, and Fast Measurement and Analysis of Nanoparticle Morphology from Transmission Electron Microscopy (Tem) Micrographs. *Nanoscale* **2012**, *4*, 5356−5372.
(32) Hyeon, T.; Lee, S. S.; Park, J.; Chung, Y.; Na, H. B. Synthesis of Highly Crystalline and Monodisperse Maghemite Nanocrystallites without a Size-Selection Process. *J. Am. Chem. Soc.* **2001**, *123*, 12798−12801.
(33) Park, J.; An, K.; Hwang, Y.; Park, J.-G.; Noh, H.-J.; Kim, J.-Y.; Park, J.-H.; Hwang, N.-M.; Hyeon, T. Ultra-Large-Scale Syntheses of Monodisperse Nanocrystals. *Nat. Mater.* **2004**, *3*, 891−895.
(34) Napolitano, A.; D'Ischia, M.; Costantini, C.; Prota, G. A New Oxidation Pathway of the Neurotoxin 6-Aminodopamine. Isolation and Characterization of a Dimer with a Tetrahydro[3,4a]-Iminoethanophenoxazine Ring System. *Tetrahedron* **1992**, *48*, 8515−8522.
(35) Bixner, O.; Lassenberger, A.; Baurecht, D.; Reimhult, E. Complete Exchange of the Hydrophobic Dispersant Shell on Monodisperse Superparamagnetic Iron Oxide Nanoparticles. *Langmuir* **2015**, *31*, 9198−9204.
(36) El-Faham, A.; Funosas, R. S.; Prohens, R.; Albericio, F. Comu: A Safer and More Effective Replacement for Benzotriazole-Based Uronium Coupling Reagents. *Chem. - Eur. J.* **2009**, *15*, 9404−9416.
(37) Riemer, J.; Hoepken, H. H.; Czerwinska, H.; Robinson, S. R.; Dringen, R. Colorimetric Ferrozine-Based Assay for the Quantitation of Iron in Cultured Cells. *Anal. Biochem.* **2004**, *331*, 370−375.
(38) Glauert, A. M.; Lewis, P. R. *Biological Specimen Preparation for Transmission Electron Microscopy*, 2nd ed.; Princeton University Press: Princeton, NJ, 1999.
(39) Laemmli, U. K. Cleavage of Structural Proteins During the Assembly of the Head of Bacteriophage T4. *Nature* **1970**, *227*, 680−685.
(40) Thornback, C. J. J. *Medicinal Applications of Coordination Chemistry*, 1st ed.; RSC: Cambridge, U.K., 2007.
(41) Finger, L. W.; Hazen, R. M.; Hofmeister, A. M. High-Pressure Crystal Chemistry of Spinel (MgAl2O4) and Magnetite (Fe3O4): Comparisons with Silicate Spinels. *Phys. Chem. Miner.* **1986**, *13*, 215−220.
(42) de Haan, H. W.; Paquet, C. Enhancement and Degradation of the R-2* Relaxation Rate Resulting from the Encapsulation of Magnetic Particles with Hydrophilic Coatings. *Magn. Reson. Med.* **2011**, *66*, 1759−1766.
(43) Gillis, P.; Moiny, F.; Brooks, R. A. On T(2)-Shortening by Strongly Magnetized Spheres: A Partial Refocusing Model. *Magn. Reson. Med.* **2002**, *47*, 257−263.
(44) Brooks, R. A.; Moiny, F.; Gillis, P. On T2-Shortening by Weakly Magnetized Particles: The Chemical Exchange Model. *Magn. Reson. Med.* **2001**, *45*, 1014−1020.
(45) Paquet, C.; de Haan, H. W.; Leek, D. M.; Lin, H.-Y.; Xiang, B.; Tian, G.; Kell, A.; Simard, B. Clusters of Superparamagnetic Iron Oxide Nanoparticles Encapsulated in a Hydrogel: A Particle Architecture Generating a Synergistic Enhancement of the T-2 Relaxation. *ACS Nano* **2011**, *5*, 3104−3112.
(46) Amstad, E.; Fischer, H.; Gehring, A. U.; Textor, M.; Reimhult, E. Magnetic Decoupling of Surface Fe3+ in Magnetite Nanoparticles Upon Nitrocatechol-Anchored Dispersant Binding. *Chem. - Eur. J.* **2011**, *17*, 7396−7398.
(47) Amstad, E.; Gehring, A. U.; Fischer, H.; Nagaiyanallur, V. V.; Haehner, G.; Textor, M.; Reimhult, E. Influence of Electronegative Substituents on the Binding Affinity of Catechol-Derived Anchors to Fe(3)O(4) Nanoparticles. *J. Phys. Chem. C* **2011**, *115*, 683−691.
(48) Luigjes, B.; Woudenberg, S. M. C.; de Groot, R.; Meeldijk, J. D.; Torres Galvis, H. M.; de Jong, K. P.; Philipse, A. P.; Erne, B. H. Diverging Geometric and Magnetic Size Distributions of Iron Oxide Nanocrystals. *J. Phys. Chem. C* **2011**, *115*, 14598−14605.
(49) Kim, J.; Piao, Y.; Hyeon, T. Multifunctional Nanostructured Materials for Multimodal Imaging, and Simultaneous Imaging and Therapy. *Chem. Soc. Rev.* **2009**, *38*, 372−390.
(50) Wang, W.; Ji, X.; Na, H. B.; Safi, M.; Smith, A.; Palui, G.; Perez, J. M.; Mattoussi, H. Design of a Multi-Dopamine-Modified Polymer Ligand Optimally Suited for Interfacing Magnetic Nanoparticles with Biological Systems. *Langmuir* **2014**, *30*, 6197−6208.
(51) Amstad, E.; Zurcher, S.; Mashaghi, A.; Wong, J. Y.; Textor, M.; Reimhult, E. Surface Functionalization of Single Superparamagnetic Iron Oxide Nanoparticles for Targeted Magnetic Resonance Imaging. *Small* **2009**, *5*, 1334−1342.
(52) Liu, D.-F.; Wu, W.; Ling, J.-J.; Wen, S.; Gu, N.; Zhang, X.-Z. Effective PEGylation of Iron Oxide Nanoparticles for High Performance in Vivo Cancer Imaging. *Adv. Funct. Mater.* **2011**, *21*, 1498−1504.
(53) Xie, J.; Xu, C.; Kohler, N.; Hou, Y.; Sun, S. Controlled Pegylation of Monodisperse Fe3o4 Nanoparticles for Reduced Non-Specific Uptake by Macrophage Cells. *Adv. Mater.* **2007**, *19*, 3163−3166.
(54) Gruenewald, T. A.; Lassenberger, A.; van Oostrum, P. D. J.; Rennhofer, H.; Zirbs, R.; Capone, B.; Vonderhaid, I.; Amenitsch, H.; Lichtenegger, H. C.; Reimhult, E. Core-Shell Structure of Monodisperse Poly(Ethylene Glycol)-Grafted Iron Oxide Nanoparticles Studied by Small-Angle X-Ray Scattering. *Chem. Mater.* **2015**, *27*, 4763−4771.
(55) Poselt, E.; Kloust, H.; Tromsdorf, U.; Janschel, M.; Hahn, C.; Masslo, C.; Weller, H. Relaxivity Optimization of a PEGylated Iron-Oxide-Based Negative Magnetic Resonance Contrast Agent for T2-Weighted Spin-Echo Imaging. *ACS Nano* **2012**, *6*, 1619−1624.
(56) Maity, D.; Zoppellaro, G.; Sedenkova, V.; Tucek, J.; Safarova, K.; Polakova, K.; Tomankova, K.; Diwoky, C.; Stollberger, R.; Machala, L.; Zboril, R. Surface Design of Core-Shell Superparamagnetic Iron Oxide Nanoparticles Drives Record Relaxivity Values in Functional Mri Contrast Agents. *Chem. Commun.* **2012**, *48*, 11398−11400.
(57) Leal, M. P.; Munoz-Hernandez, C.; Berry, C. C.; Garcia-Martin, M. L. In Vivo Pharmacokinetics of T2 Contrast Agents Based on Iron Oxide Nanoparticles: Optimization of Blood Circulation Times. *RSC Adv.* **2015**, *5*, 76883−76891.
(58) Park, Y. C.; Smith, J. B.; Pham, T.; Whitaker, R. D.; Sucato, C. A.; Hamilton, J. A.; Bartolak-Suki, E.; Wong, J. Y. Effect of Peg Molecular Weight on Stability, T2 Contrast, Cytotoxicity, and Cellular Uptake of Superparamagnetic Iron Oxide Nanoparticles (Spions). *Colloids Surf., B* **2014**, *119*, 106−114.
(59) Gal, N.; Lassenberger, A.; Herrero-Nogareda, L.; Scheberl, A.; Charwat, V.; Kasper, C.; Reimhult, E. Interaction of Size-Tailored Pegylated Iron Oxide Nanoparticles with Lipid Membranes and Cells. *ACS Biomater. Sci. Eng.* **2016**, Article ASAP. DOI: 10.1021/acsbiomaterials.6b00311.
(60) Almonte, L.; Lopez-Elvira, E.; Baró, A. M. Surface-Charge Differentiation of Streptavidin and Avidin by Atomic Force Microscopy−Force Spectroscopy. Chem. Phys. *ChemPhysChem* **2014**, *15*, 2768−2773.
(61) Wang, C.; Sun, A.; Qiao, Y.; Zhang, P.; Ma, L.; Su, M. Cationic Surface Modification of Gold Nanoparticles for Enhanced Cellular Uptake and X-Ray Radiation Therapy. *J. Mater. Chem. B* **2015**, *3*, 7372−7376.
(62) Luo, R.; Neu, B.; Venkatraman, S. S. Surface Functionalization of Nanoparticles to Control Cell Interactions and Drug Release. *Small* **2012**, *8*, 2585−2594.

DOI: 10.1021/acsami.6b12932
ACS Appl. Mater. Interfaces 2017, 9, 3343−3353